Generalized cable formalism to calculate the magnetic field of single neurons and neuronal populations

Claude Bedard and Alain Destexhe

UNIC, CNRS, F-91198 Gif-sur-Yvette, France

Neurons generate magnetic fields which can be recorded with macroscopic techniques such as magnetoencephalography. The theory that accounts for the genesis of neuronal magnetic fields involves dendritic cable structures in homogeneous resistive extracellular media. Here we generalize this model by considering dendritic cables in extracellular media with arbitrarily complex electric properties. This method is based on a multiscale mean-field theory where the neuron is considered in interaction with a "mean" extracellular medium (characterized by a specific impedance). We first show that, as expected, the generalized cable equation and the standard cable generate magnetic fields that mostly depend on the axial current in the cable, with a moderate contribution of extracellular currents. Less expected, we also show that the nature of the extracellular and intracellular media influence the axial current, and thus also influence neuronal magnetic fields. We illustrate these properties by numerical simulations and suggest experiments to test these findings.

I. INTRODUCTION

Neuronal magnetic activity is usually measured through magnetoencephalogram (MEG) signals, which are recorded by using sensitive Superconducting Quantum Interference Device (SQUID) detectors. These sensors operate at very low temperatures (4 K) and must necessarily be located centimeters away from the human scalp [1]. Because of the macroscopic aspect of SQUID measurements, it is usually assumed that the underlying sources are "macroscopic dipoles" produced by the synchronized activity of thousand of neurons in a small region of cortex [2].

However, over the last few years, many efforts have been devoted to building magnetic sensors of another kind, which are based on the giant magneto-resistance (GMR) effect in spin electronics [3]. Such sensors have the advantage of being able to work at physiological temperatures, and they can be miniaturized, so it is possible to build "magnetrodes" [4], the magnetic equivalent of a micro-electrode. Such devices are aimed to record microscopically, the activity of a small group of neurons. While the theory exists for macroscopic SQUID measurements and macroscopic neuronal sources [2], the theory to explain the genesis of magnetic fields by single neurons has been very scarcely developed [5]. This is the first motivation of the present study.

The second motivation follows from a controversy in the literature about the role and properties of the extracellular medium around neurons [6,7]. The "standard" model of the genesis of the extracellular local field potential (LFP) assumes that the neurons are dipolar sources embedded in a resistive (Ohmic) extracellular medium. While some measurements seem to confirm this hypothesis [8], other measurements revealed a marked frequency dependence of the extracellular resistivity [9,10], which indicates that the medium is nonresistive or non-Ohmic.[1] Indirect measurements of the extracellular impedance, as well as the spectral analysis of LFP signals, also indicate deviations from resistivity [11–14]. Such deviations can be explained by phenomena like ionic diffusion [15], which reproduce the correct frequency scaling of LFP signals. In addition, there is also evidence [16] that multipolar components are not sufficient to explain the data, but that a strong monopolar component should be taken into account.

These controversies have important consequences, because if the extracellular medium is nonresistive, several fundamental theories of neural dynamics, such as the well-known cable theory of neurons [17,18] or the current-source density analysis [19], are incorrect and need to be reformulated accordingly [15,20]. The same considerations may also hold for the genesis of the magnetic fields, as the current theory [2] also assumes that the medium is resistive.

In the present paper, our aim is to build a neuron model to generate electromagnetic fields based on first principles and that does not make any *a priori* assumption, such as the nature of the impedance of the extracellular medium. However, to this end, we cannot use the classic cable formalism, which was initially developed by Rall [17]. Although this formalism has been one of the most successful formalism of theoretical neuroscience, explaining a large range of phenomena [18,21–23], it is nonvalid to describe neurons in nonresistive media. To palliate this difficulty, we have recently generalized cable theory to make it valid for neurons embedded in media with arbitrarily complex electrical properties [20]. In the present framework, we will use this generalized cable theory which will be extended to calculate neuronal magnetic induction and electric potential in extracellular space.

We start by outlining a generalized theoretical formalism to calculate the magnetic field around neurons, and we next illustrate this formalism by using numerical simulations.

II. THEORY

In this section, we develop a mean-field method to evaluate the magnetic induction $\vec{B}$ produced by one neuron or by a population of neurons, based on the Maxwell theory of electromagnetism.

---

[1]In a non-Ohmic medium, the differential Ohm's law ($\vec{j}^f = \sigma \vec{E} =$ const$\times \vec{E}$) does not apply.

In a first step, we start from Maxwell equations in a mean field [15] and in Fourier frequency space to derive the differential equation for the magnetic induction $\vec{B}$. Note that in principle, one should use the notation $\langle\vec{B}\rangle$ for the spatial arithmetic average of $\vec{B}$, but in the rest of the paper we will use the notation $\vec{B}$ for simplicity. The same convention will be used for the other quantities such as the magnetic field $\vec{H}$, electric field $\vec{E}$, electric displacement $\vec{D}$, electric potential V, magnetic vector potential $\vec{A}$, free-charge current density $\vec{j}^f$, generalized current density $\vec{j}^g$ [20], and impedance of the extracellular medium z_{medium}. Note that taking the spatial arithmetic average of the medium impedance implies to take the harmonic mean over the medium admittance γ, because we have $z_{medium} = 1/\gamma = 1/(\sigma + i\omega\varepsilon)$.

In a second step, we evaluate $\vec{B}$ produced by a cylinder compartment embedded in a complex extracellular medium. We begin by calculating the boundary conditions of $\vec{B}$ on the surface of the cylinder compartment. This method uses the same approach results that we recently introduced and applied to calculate the transmembrane electric potential in the same model [20]. This method will be used to calculate the boundary conditions of $\vec{B}$, and these boundary conditions will then be used to obtain an explicit solution of the differential equation that $\vec{B}$ must satisfy. Next, we will explicitly calculate the field $\vec{B}$.

In a third step, we use these results together with the superposition principle to obtain a general method to calculate the field $\vec{B}$ produced by a large number of cylinder compartments, which can define either a single-neuron dendritic morphology or a population of neurons.

A. Differential equation for $\vec{B}$

We now derive the differential equation for $\vec{B}$ in a mean field and in an extracellular medium which is linear, heterogeneous, and scalar.[2] In such media, we consider the general case where there can be formation of ions, through chemical reactions. Such charge creation or annihilation will determine additional current densities. At any time, we have

$$\rho^{c+} + \rho^{c-} = 0$$
$$\vec{j}^c = \vec{j}^+ + \vec{j}^- = \rho^{c+}\vec{v}^+ + \rho^{c-}\vec{v}^-,$$

where ρ^{c+} and ρ^{c-} are the variations of positive and negative charge densities, produced by chemical reactions in a given volume. These relations express the fact that the free-charge density remains constant when we have creation and annihilation of ions, but that the nonconservation of the total number of ions determines, in general, a current density of charge creation $\vec{j}^c$ (because $\vec{j}^+$ and $\vec{j}^-$ necessarily have the same sign).

In such a case, according to classic electromagnetism theory, charge densities and current densities are linked by

two sets of equations. The first set comprises four operatorial equations:

$$\vec{\nabla} \cdot \vec{D}(\vec{x},\omega) = \rho^f(\vec{x},\omega) \quad \text{(i)}$$
$$\vec{\nabla} \times \vec{E}(\vec{x},\omega) = -i\omega\vec{B}(\vec{x},\omega) \quad \text{(ii)}$$
$$\vec{\nabla} \cdot \vec{B}(\vec{x},\omega) = 0 \quad \text{(iii)}$$
$$\vec{\nabla} \times \vec{H}(\vec{x},\omega) = \vec{j}^g(\vec{x},\omega) + \vec{j}^c(\vec{x},\omega) \quad \text{(iv)}. \quad (1)$$

Note that $\vec{j}^g = \vec{j}^f + i\omega\vec{D}$ [Eq. 1(iv)]. where $\vec{j}^f$ is the free-charge current density and $i\omega\vec{D}$ is the displacement current density.

A second set of equations comprises the two linking equations between $\vec{D}$ and $\vec{E}$, as well as $\vec{H}$ and $\vec{B}$ interaction fields, and one linking equation between the free-charge current density field $\vec{j}^f$ and $\vec{E}$. Experiments [10,24] and theory [25] have shown that these linking equations can be represented by the following convolution equations:

$$\vec{D}(\vec{x},\omega) = \varepsilon(\vec{x},\omega)\vec{E}(\vec{x},\omega) \quad \text{(i)}$$
$$\vec{B}(\vec{x},\omega) = \mu(\vec{x},\omega)\vec{H}(\vec{x},\omega) \quad \text{(ii)} \quad (2)$$
$$\vec{j}^f(\vec{x},\omega) = \sigma(\vec{x},\omega)\vec{E}(\vec{x},\omega) \quad \text{(iii)}$$

for a linear and scalar medium. Note that all of the above was formulated in Fourier frequency space.

Assuming that if the base volume considered in the mean-field analysis is large enough, we have at any time the same number of creation and annihilation of ions, and we can write $\vec{j}^c(\vec{x},t) \approx 0$, so that the Fourier transform of $\vec{j}^c(\vec{x},t)$ can be considered zero for physiological frequencies.[3] This is equivalent to consider that the current fluctuations caused by chemical reactions are negligible. It follows from Eqs. 1(iii) and 1(iv):

$$\vec{\nabla}\times(\vec{\nabla}\times\vec{B}) = -\nabla^2\vec{B} + \vec{\nabla}(\vec{\nabla}\cdot\vec{B}) = -\nabla^2\vec{B} = \mu_o\vec{\nabla}\times\vec{j}^g, \quad (3)$$

where $\vec{j}^g$ is the generalized current density. This current can be expressed as $\vec{j}^g = \gamma\vec{E} = (\sigma + i\omega\varepsilon)\vec{E}$, where γ is the admittance of the scalar medium (in a mean field;[4] see also the linking equations [Eqs. (2)]). If the volume of the mean-field formalism is large enough, the admittance does not depend on spatial position, and we can write

$$\vec{\nabla}\times\vec{j}^g = \gamma\vec{\nabla}\times\vec{E} = -i\omega\gamma\vec{B}. \quad (4)$$

---

[2]Note that by definition, a given medium *linear* when the linking equations between the fields are convolution products that do not depend on the field intensities. A medium is *scalar* when the parameters in the convolution products do not depend on direction in space (i.e., are isotropic), which is a good approximation in a mean-field theory.

[3]Note that it is clear that one can have fluctuations of the number of ions per unit volume, independently of the size considered, when the time interval is sufficiently small. However, such contributions will necessarily participate to very high frequencies in the variation of $\vec{j}^c(\vec{x},\omega)$, which are well outside the "physiological" range of measurable frequencies in experiments (about 1–1000 Hz).

[4]Note that in a mean-field theory, the electromagnetic parameters are calculated for a given volume and therefore do not depend on spatial coordinates (for a sufficiently large volume). However, the renormalization to obtain the "macroscopic" electric parameters results in a frequency dependence of these parameters. This occurs if electric parameters are not spatially uniform at microscopic scales or from processes such as ionic diffusion, polarization, etc. [15,26,27].
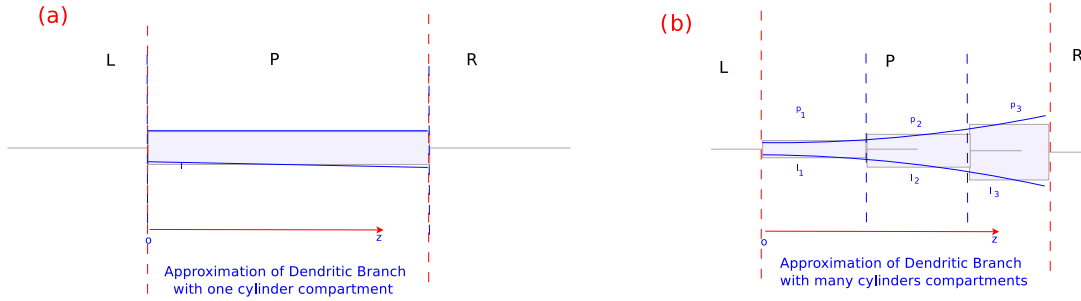
FIG. 1. (Color online) Scheme to calculate the magnetic induction produced by a dendritic branch. (a) To evaluate the contribution of the dendritic segment, we divide space into three regions: L, P, R. We first evaluate $\mathbf{B}^\theta$ in the principal region P, which corresponds to the space between Regions L and R. Next, we evaluate $\mathbf{B}^\theta$ in the boundary regions L and R. Note that the knowledge of $\mathbf{B}^\theta$ in Region P is necessary to evaluate $\mathbf{B}^\theta$ in Regions L and R because one must know $\mathbf{B}^\theta$ on the two planes $z = 0$ and $z = \sum_{i=1}^{N_p} l_i = l$, in order to calculate its explicit value in Regions L and R using Eq. (5). (b) Evaluation of $\mathbf{B}^\theta$ for a segment of variable diameter. In this case, the same procedure is followed, except that Region P is divided into N_p compartments, each described by a continuous cylinder, $P = \bigcup_{i=1}^{N_p} p_i$. Note that the continuity conditions on the axial current and the transmembrane voltage allow one to define boundary conditions for $\mathbf{B}^\theta$ over the surfaces of the compartments p_i. The figure shows an example with $N_p = 3$.

It follows that

$$\nabla^2 \vec{\mathbf{B}} = i\omega\mu_o\gamma\vec{\mathbf{B}}. \tag{5}$$

Thus, one sees that in general, the differential equation for $\vec{\mathbf{B}}$ depends on the admittance of the medium γ. This is due to the fact that we have considered $\vec{\nabla}\times\vec{\mathbf{j}}^g \neq 0$ in Eq. (4), which is equivalent to allow electromagnetic induction to occur.

We will see later that, for physiological frequencies, the right-hand term of Eq. (5) is negligible, so that we can in practice calculate $\vec{\mathbf{B}}$ very accurately using the expression $\nabla^2\vec{\mathbf{B}} = 0$. Note that this approximation amounts to neglect electromagnetic induction effects in the context of natural neurophysiological phenomena of low frequency (<1000 Hz) because the right-hand side of Eq. (5) originates in the mathematic formalization of electromagnetic induction [Faraday-Maxwell law, Eq. 1(ii)]. However, it is important to keep in mind that the right-hand term in Eq. (5) cannot be neglected in the presence of magnetic stimulation [28], because this technique uses electromagnetic induction to induce currents in biological media. Therefore, when considering magnetic stimulation, we will need to update this formalism accordingly.

B. Evaluation of $\vec{\mathbf{B}}$

In the preceding section, we have determined the differential equation that $\vec{\mathbf{B}}$ must satisfy in Fourier frequency space.
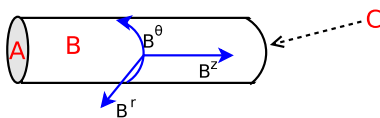

FIG. 2. (Color online) Coordinate scheme for a cable segment of constant diameter. The scheme shows the cable with the cylindric coordinate system used in the paper, as well as the surfaces A and C, which are the sections that cuts the cable perpendicular to its membrane (delimited by surface B). $\mathcal{D}$ is the interior volume of the segment, as delimited by these surfaces, and $\partial\mathcal{D}$ is the reunion of the two surfaces A and B.

Note that the linearity of Eq. (5) implies that its solution for a given frequency does not depend on other frequencies (which would not be true if the equation was nonlinear). However, this equation is not sufficient to determine $\vec{\mathbf{B}}$ because the boundary conditions must be known to obtain an explicit solution. To solve this boundary condition problem, we must use cable equations because we consider the "microscopic" case where the electromagnetic field results from the activity of each individual neuron, rather than considering "macroscopic" sources representing the activity of thousands of neurons as traditionally done. Moreover, to keep the formalism as general as possible, we consider the "generalized cable equations" [20], which generalizes the classic cable equations of Rall [17,18] to the general situation where the extracellular medium can have complex or inhomogeneous electrical properties. We will also use a similar method of continuous cylinder compartment as introduced previously [20].[5]

In the following, we first calculate the boundary conditions for an arbitrary cylinder compartment (with arbitrary length and diameter) [20]. We will see that it is sufficient to evaluate the generalized axial current i_i^g inside each continuous cylinder compartment to evaluate its boundary conditions. Second, we consider the more realistic scenario of a dendritic branch of variable diameter, which is approximated by continuous cylinder compartments (Fig. 1). We then calculate everywhere in space the value of $\vec{\mathbf{B}}$ produced by this dendritic branch. Finally, we give a general description of the computation of $\vec{\mathbf{B}}$ produced by several dendritic branches. This description can apply in general to any dendritic morphology, or axons, from one or several neurons.

---

[5]The method of continuous cylinder compartments consists of solving analytically the cable equations in a continuous cylindric cable compartment, which can be of arbitrary length, but constant diameter (see details in Ref. [20]).

1. Boundary conditions of $\vec{B}$ for a continuous cylinder compartment

We now calculate the boundary conditions of $\vec{B}$ on the surface of a continuous cylinder compartment. To do this, we set $\vec{B} = \mathbf{B}^\theta \hat{e}^\theta$ because we have a complete cylindric symmetry (see details in Appendix A). Once the direction of $\vec{B}$ is known, one can calculate the boundary conditions of $\vec{B}$ using Ampère-Maxwell's law.

We now evaluate $\mathbf{B}^\theta$ as a function of the generalized current. We calculate the values of $\mathbf{B}^\theta$ as a function of the generalized current over the surface $\mathcal{S}_B$ (Fig. 2) using Ampère-Maxwell law [Eq. (1)iv]. We obtain

$$\oint_{\partial \mathcal{S}_B} \vec{B} \cdot d\vec{s} = \iint_{\mathcal{S}_A} \vec{\nabla} \times \vec{B} \cdot \hat{n}_{\mathcal{S}_A} \, dS$$

$$= \mu_o \iint_{\mathcal{S}_A} \vec{j}^g \cdot \hat{n}_{\mathcal{S}_A} \, dS = \mu_o i_i^g, \qquad (6)$$

where i_i^g is the generalized axial current inside the continuous cylinder compartment. Taking into account cylindric symmetry gives

$$\vec{B} = \mathbf{B}^\theta \hat{e}_\theta = \frac{\mu_o i_i^g(z,\omega)}{2\pi a} \hat{e}_\theta, \qquad (7)$$

where i_i^g is the axial current inside the compartment and a is its radius.

This equation together with Eq. (5) shows that the value of $\vec{B}$ around a dendritic compartment will depend on the impedance of the extracellular medium ($1/\gamma$) for two different reasons. First, the right-hand term of Eq. (5) explicitly depends on the extracellular impedance, but we will see in the next section that these electromagnetic induction effects are likely to be negligible. Second, Eq. (7) shows that the boundary conditions also depend on the extracellular impedance, because the spatial and frequency profiles of i_i^g depend on this impedance [20]. However, we will see that, contrary to electromagnetic induction, this dependency cannot be neglected when calculating $\vec{B}$, because this effect is potentially important. In the next section, we calculate magnetic induction in the extracellular space by directly solving Eq. (5) using the boundary conditions evaluated by Eq. (7).

2. General expression of $\vec{B}$ in extracellular space for a dendritic branch

In this section, we derive a method to calculate the expression of $\vec{B}$ for a dendritic branch (Fig. 1) In cylindric coordinates, Eq. (5) writes

$$\nabla^2 \vec{B} = \left[\frac{\partial^2 \mathbf{B}^r}{\partial r^2} + \frac{1}{r^2} \frac{\partial^2 \mathbf{B}^r}{\partial \theta^2} + \frac{\partial^2 \mathbf{B}^r}{\partial z^2} + \frac{1}{r} \frac{\partial \mathbf{B}^r}{\partial r} - \frac{2}{r^2} \frac{\partial \mathbf{B}^\theta}{\partial \theta} - \frac{\mathbf{B}^r}{r^2} \right] \hat{\mathbf{e}}_\mathbf{r} \cdots$$

$$+ \left[\frac{\partial^2 \mathbf{B}^\theta}{\partial r^2} + \frac{1}{r^2} \frac{\partial^2 \mathbf{B}^\theta}{\partial \theta^2} + \frac{\partial^2 \mathbf{B}^\theta}{\partial z^2} + \frac{1}{r} \frac{\partial \mathbf{B}^\theta}{\partial r} + \frac{2}{r^2} \frac{\partial \mathbf{B}^r}{\partial \theta} - \frac{\mathbf{B}^\theta}{r^2} \right] \hat{\mathbf{e}}_\theta \cdots$$

$$+ \left[\frac{\partial^2 \mathbf{B}^z}{\partial r^2} + \frac{1}{r^2} \frac{\partial^2 \mathbf{B}^z}{\partial \theta^2} + \frac{\partial^2 \mathbf{B}^z}{\partial z^2} + \frac{1}{r} \frac{\partial \mathbf{B}^z}{\partial r} \right] \hat{\mathbf{e}}_\mathbf{z} = i\omega\mu_o\gamma\vec{B} = i\omega\mu_o\gamma[\mathbf{B}^r \hat{\mathbf{e}}_\mathbf{r} + \mathbf{B}^\theta \hat{\mathbf{e}}_\theta + \mathbf{B}^z \hat{\mathbf{e}}_\mathbf{z}]. \qquad (8)$$

According to the preceding section, the boundary conditions imply $\vec{B} = \mathbf{B}^\theta(r,z)\hat{e}_\theta$ on the surface of each continuous cylinder compartment, as well as $\vec{B} = 0$ for infinite distances. The cylindric symmetry of the boundary conditions implies that $\mathbf{B}^r = \mathbf{B}^z = 0$ everywhere in space because the solution of Eq. (8) is unique. Consequently, to evaluate the value of $\mathbf{B}^\theta$ produced by a dendritic branch, one must solve the following equation:

$$\frac{\partial^2 \mathbf{B}^\theta}{\partial r^2} + \frac{1}{r} \frac{\partial \mathbf{B}^\theta}{\partial r} + \frac{\partial^2 \mathbf{B}^\theta}{\partial z^2} - \frac{\mathbf{B}^\theta}{r^2} = i\omega\mu_o\gamma\mathbf{B}^\theta. \qquad (9)$$

3. Solving the equation of $\vec{B}$ for a continuous cylinder compartment

In this section, we present an iterative method to calculate the solution of Eq. (9) in natural conditions (in the absence of electric or magnetic stimulation) and for a continuous cylinder compartment of radius a and length l, when the values of $\mathbf{B}^\theta$ on its surface are known. To do this, we neglect electromagnetic induction and set the right term of Eq. (9) $i\omega\mu_o\gamma\mathbf{B}$ to zero, because we have $\omega\mu_o|\gamma| \approx 0$ for the typical size of a neuron in cerebral cortex, and for frequencies lower than about 1000 Hz. Indeed $\mu_o = 4\pi \times 10^{-7}$ H/m, and the admittance of the extracellular medium is certainly lower than that of sea

water, and thus we can write $|\gamma_{\text{medium}}| < |\gamma_{\text{sea water}}| < 1$, and if we consider that $r_{\text{cortex}} \ll r_{\text{max}} = 1$ m, then we have $k^2 + 1/r^2 > 1/r_{\text{max}}^2 = 1 \gg \omega\mu_0|\gamma|$. This approximation amounts to neglect the phenomenon of electromagnetic induction (in the absence of magnetic stimulation). Thus, the frequency dependence of $\vec{B}$ is essentially caused by the frequency dependence of the axial current i_i^g. Note that i_i^g depends on the nature of extracellular and cytoplasm impedances, as shown previously in the generalized cable [20].

The goal of this approach is to provide a method to solve Laplace's equation ($\nabla^2\vec{B} = 0$) in three dimensions, assuming a perfect cylindric symmetry of the dendritic compartment. This approach allows one to reduce the problem to two dimensions.[6] We approach the solution of this problem by using an iterative method. The idea of the method is to calculate, in a first step, the solution using complex Fourier transform, which gives an exact solution for an infinite cylinder. This first estimate is then corrected by successive iterations using the

---

[6]Note that Laplace's equation can also be solved using the finite element method for a simple geometry. For example, the Galerkin [29] method works very well in this case but requires significant computation time compared to a two-dimensional method.
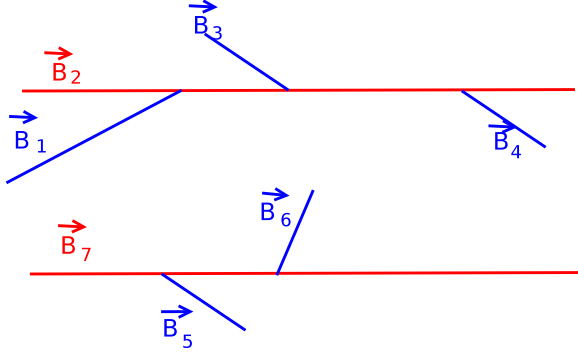
FIG. 3. (Color online) Example with two neurons. In order to calculate the value of the magnetic induction $\vec{\mathbf{B}}$ generated by many neurons, one has to sum the values of $\vec{\mathbf{B}}_i$ produced by each branch. Thus, it is sufficient to know the axial current i_i^g at each branch to calculate $\vec{\mathbf{B}}$.

first-order Hankel transform. This method is presented in detail in Appendix B, while in Appendix C we demonstrate that the method converges.

4. The general expression of $\vec{\mathbf{B}}$ for N_B dendritic branches from one or several neurons

Assuming that electromagnetic induction is negligible, and that the medium is linear, we can apply the superposition principle such that we can write $\vec{\mathbf{B}}$ as

$$\vec{\mathbf{B}} = \sum_{i=1}^{N_B} \vec{\mathbf{B}}_i, \qquad (10)$$

where each $\vec{\mathbf{B}}_i$ is the magnetic induction produced by each branch as if it was isolated.

Thus, at some distance away of an ensemble of dendritic branches assimilable to continuous cylinder compartments (Fig. 3), the field $\vec{\mathbf{B}}$ is the vectorial sum of the field $\vec{\mathbf{B}}$ produced by each compartment, which is itself calculated from the average spatial and frequency profile of the axial current in each compartment (see Sec. II B 3).

C. Importance of the spatial profile of the axial current

In the previous section, we have calculated $\vec{\mathbf{B}}$ without explicitly considering the current in the extracellular space around the neuron. However, we know that this current necessarily produces a magnetic induction, and thus it is necessary to include this contribution to obtain a complete evaluation of $\vec{\mathbf{B}}$ in extracellular space. In this section, we show that that this contribution of extracellular currents is implicitly taken into account by our formalism, through the spatial and frequency profile of i_i^g.

According to Eqs. 1 (iv) and 2 (ii), we can evaluate the generalized current outside of a continuous cylinder compartment:

$$\vec{\mathbf{j}}^g = \frac{1}{\mu_o} \vec{\nabla} \times \vec{\mathbf{B}} \qquad (11)$$

when $\vec{\mathbf{j}}^c = 0$ and for $\mu(\vec{x},\omega) = \mu_o$. Rewriting this expression in cylindric coordinates, we obtain

$$\vec{\mathbf{j}}^g = \frac{1}{\mu_o} \left\{ \left(\frac{1}{r} \frac{\partial \mathbf{B}^z}{\partial \theta} - \frac{\partial \mathbf{B}^\theta}{\partial z} \right) \hat{e}_r + \left(\frac{\partial \mathbf{B}^r}{\partial z} - \frac{\partial \mathbf{B}^z}{\partial r} \right) \hat{e}_\theta \right.$$
$$\left. + \frac{1}{r} \left[\frac{\partial (r \mathbf{B}^\theta)}{\partial r} - \frac{\partial \mathbf{B}^r}{\partial \theta} \right] \hat{e}_z \right\}. \qquad (12)$$

It follows that

$$\vec{\mathbf{j}}^g = \frac{1}{\mu_o} \left[-\frac{\partial \mathbf{B}^\theta}{\partial z} \hat{e}_r + \left(\frac{\partial \mathbf{B}^\theta}{\partial r} + \frac{\mathbf{B}^\theta}{r} \right) \hat{e}_z \right] \qquad (13)$$

because the solution is of the form $\vec{\mathbf{B}}(r,\theta,z,\omega) = \mathbf{B}^\theta(r,z,\omega)\hat{e}_\theta$ (Sec. II B 2). We see that the generalized current density outside of the neuron is different from zero, if and only if we have

$$-\frac{\partial \mathbf{B}^\theta}{\partial z} \neq 0$$
$$\frac{\partial \mathbf{B}^\theta}{\partial r} + \frac{\mathbf{B}^\theta}{r} \neq 0 \qquad (14)$$

Thus, the external current around the neuron is taken into account because the solution depends on r and z in general (see the preceding section).

Note that we have $\frac{\partial \mathbf{B}^\theta}{\partial z} = 0$ (Fig. 1) if and only if the spatial profile of the axial current i_i^g does not depend on z [Eq. (7)]. In this case, the current i_m is zero, which implies that the electric field produced by the compartment is also zero [17,18,20]. In addition, we know that in a neuron, one cannot have axial current without transmembrane current, and, thus, it is impossible that $\frac{\partial \mathbf{B}^\theta}{\partial z} = 0$ in a given compartment. Therefore, we can conclude that the external current is taken into consideration because $\vec{\nabla} \times \vec{\mathbf{B}} \neq 0$ outside of the compartment when $\vec{\mathbf{B}}$ depends on z.

In the preceding section, we have calculated $\mathbf{B}^\theta$ for a single continuous cylinder compartment. We now consider the more complex case when this compartment is connected to a soma on one side, according to a "ball-and-stick" configuration. In this case, one can consider that the current density $\vec{\mathbf{j}}^g$ in Region R satisfies $\vec{\nabla} \cdot \vec{\mathbf{j}}^g = 0$ (the generalized current conservation law) when $\vec{\mathbf{j}}^c = 0$ and

$$\vec{\nabla} \times \vec{\mathbf{j}}^g = (\sigma_e + i\omega\varepsilon)\vec{\nabla} \times \vec{\mathbf{E}} = 0$$

(when electromagnetic induction is negligible and in a mean field).[7] It follows that we have $\nabla^2 \vec{\mathbf{j}}^g = 0$ in each point of Region R. Thus, the field $\vec{\mathbf{j}}^g$ does not explicitly depend on electromagnetic parameters. With the continuity condition of the current at the interface between Regions P and R, and the vanishing at infinite distances ($\vec{\mathbf{j}}^g \xrightarrow{\infty} 0$), we have a unique solution (Dirichlet problem) in Region R (Fig. 4).

However, the method to calculate the generalized cable for the ball-and-stick model implicitly considers the soma impedance in the spatial and frequency profiles on the

---

[7]Note that we have considered several scales in Ref. [20]: the interior of the dendritic compartment, the interior of the soma, the membrane, and the extracellular medium.
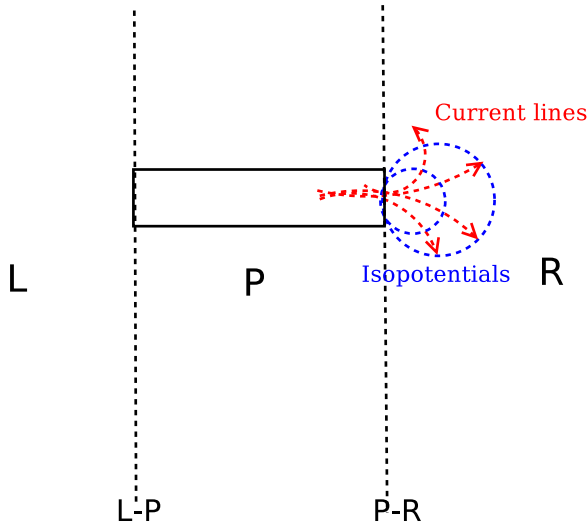
FIG. 4. (Color online) Illustration of the current fields around the soma of a ball-and-stick model. The current fields are shown (arrows) around the soma when the generalized membrane current is perpendicular to the soma membrane (red arrows). The isopotential surfaces are shown in blue and correspond to the soma membrane. If the soma has a different "diameter" but coincides with the isopotential surface, then the geometry of these current lines and isopotential surfaces remains invariant. However, the value of the electric potential is different on each equipotential surface.

continuous cylinder compartment(s) [20].[8] Thus, the soma impedance is also taken into account implicitly here when calculating the current at the interface between Regions P and R.

It is important to note that the same current geometries can be seen for different soma sizes (Fig. 4), and thus different neuron models of identical dendritic structure but different soma will generate identical magnetic inductions in Region R (comprising the soma). Note that it does not apply to the electric field and potential around the soma because we have $\vec{\mathbf{E}} = \frac{\vec{\mathbf{j}}^g}{(\sigma_e + i\omega\varepsilon)}$ where $(\sigma_e + i\omega\varepsilon)$ depends on the size of the soma membrane. Thus, the soma impedance is sufficient to determine $\vec{\mathbf{B}}$, but its exact size is not important if the soma coincides with an isopotential surface.

Consequently, taking into account the spatial and frequency profiles of $\mathbf{B}^\theta$ over the surface of the cylinder compartments allows one to calculate everywhere in space the field $\vec{\mathbf{B}}$ as well as the current fields inside and outside of the membrane. Thus, the spatial and frequency profiles of i_i^g [Eq. (7)] implicitly take into account the screening effect caused by the "return current" outside of the neuron, when present. Note that this conclusion is entirely consistent with Maxwell equations and the pseudo-parabolic equation (9) derived from it, because

---

[8]In this paper we have assumed that $\vec{\mathbf{j}}^g$ is perpendicular to the membrane surface at the soma. This implies that the internal and external surfaces of the soma are equipotential because $(\sigma_e + i\omega\varepsilon)\vec{\mathbf{E}}$ is perpendicular to the soma membrane. Thus, the soma membrane is characterized by an impedance $Z_s = \frac{V_m}{i_i^g}$, which affects the spatial and frequency profiles in the dendritic compartments.
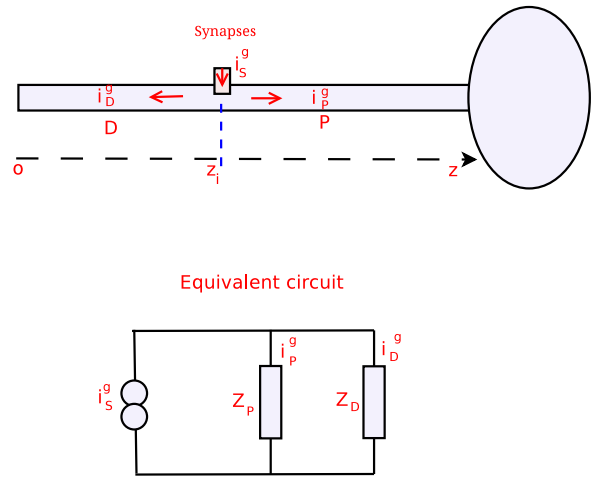

FIG. 5. (Color online) Equivalent scheme to calculate the current flowing from distal to proximal at the position of the synapse, when the synaptic current is known.

these equations determine a unique solution for a given set of boundary conditions. In the next section, we show how this method can be generalized to complex morphologies or populations of neurons (still under the condition that electromagnetic induction is negligible).

III. NUMERICAL SIMULATIONS

In this section, we show a few simulations with different types of media for a ball-and-stick type of model. In a first step, we describe how to calculate the generalized axial current as a function of the synaptic current for a ball-and-stick type of model. In a second step, we apply the method developed above to calculate the magnetic induction. We show here two examples: first, when the extracellular and cytoplasm impedances are resistive, and second, when these two impedances are diffusive (Warburg impedance).

A. Method to calculate the generalized axial current for a ball-and-stick model

In a first step, we determine the transmembrane voltage in the postsynaptic region. The current produced in this region separates in two parts: one that goes to the soma ("proximal"), and another one going in the opposite direction ("distal") (Fig. 5). These two currents are given by the relations $Z_D(z_i,\omega) = \frac{V_m(z_i,\omega)}{i_{iD}^g(z_i,\omega)}$, and $Z_P(z_i,\omega) = \frac{V_m(z_i,\omega)}{i_{iP}^g(z_i,\omega)}$, for the distal and proximal regions, respectively. These expressions were derived previously [20].

Next, we determine the equivalent impedance at the position of the synapse (Fig. 5) [20]. We obtain

$$Z_{eq}(z_i,\omega) = \frac{Z_P(z_i,\omega)Z_D(z_i,\omega)}{Z_P(z_i,\omega) + Z_D(z_i,\omega)}. \tag{15}$$

It follows that the transmembrane voltage at the position of the synapse is given by

$$V_m(z_i,\omega) = Z_{eq}(z_i,\omega)i_s^g(z_i,\omega) \tag{16}$$

when the synapse is at position z_i. Next, we determine $i_A^g(z_i, \omega)$ and $i_D^g(z_i, \omega)$ from the following expressions:

$$i_P^g(z_i, \omega) = \frac{V_m(z_i, \omega)}{Z_P(z_i, \omega)}$$

$$i_D^g(z_i, \omega) = \frac{V_m(z_i, \omega)}{Z_D(z_i, \omega)} \tag{17}$$

We have seen in Ref. [20] that with the generalized current, the cable equations can be written in a form similar to the standard cable equation:

$$\frac{\partial^2 V_m(z, \omega)}{\partial z^2} = \kappa_\lambda^2 V_m(z, \omega), \tag{18}$$

where

$$\kappa_\lambda^2 = \frac{\bar{z}_i(1 + i\omega\tau_m)}{r_m} = \frac{z_i(1 + i\omega\tau_m)}{r_m\left[1 + \frac{z_e^{(m)}}{r_m}(1 + i\omega\tau_m)\right]}, \tag{19}$$

where $1/r_m$, z_i and τ_m are, respectively, the linear density of membrane conductance (in S/m), the impedance per unit length of the cytoplasm (in [Ω/m]), and the membrane time constant. The parameter $z_e^{(m)}$ stands for the specific impedance of the extracellular medium. This parameter impacts on the spatial and frequency profile of V_m, i_m, and i_i^g and has the same units as r_m.

The general solution of this equation in Fourier space $\omega \neq 0$ is given by

$$V_{mD}(z, \omega) = A_P^+(z_i, \omega)e^{+\kappa_\lambda z} + A_D^-(z_i, \omega)e^{-\kappa_\lambda z}$$

$$V_{mP}(z, \omega) = A_P^+(z_i, \omega)e^{+\kappa_\lambda(l-z)} + A_P^-(z_i, \omega)e^{-\kappa_\lambda(l-z)} \tag{20}$$

for a continuous cylinder compartment of length l and constant diameter, and when we know the synaptic current at position $z = z_i$. In such conditions, the coefficients of Eq. (15) are given by the following expressions (see Appendix F in Ref. [20]):

$$A_D^+(z_i, \omega) = \frac{1}{2}e^{-\kappa_\lambda z_i}\left[V_{mD}(z_i, \omega) + \frac{\bar{z}_i}{\kappa_\lambda}i_{iD}^g(z_i, \omega)\right]$$

$$A_D^-(z_i, \omega) = \frac{1}{2}e^{+\kappa_\lambda z_i}\left[V_{mD}(z_i, \omega) - \frac{\bar{z}_i}{\kappa_\lambda}i_{iD}^g(z_i, \omega)\right]$$

$$A_P^+(z_i, \omega) = \frac{1}{2}e^{-\kappa_\lambda(l-z_i)}\left[V_{mP}(z_i, \omega) + \frac{\bar{z}_i}{\kappa_\lambda}i_{iP}^g(z_i, \omega)\right]$$

$$A_P^-(z_i, \omega) = \frac{1}{2}e^{+\kappa_\lambda(l-z_i)}\left[V_{mP}(z_i, \omega) - \frac{\bar{z}_i}{\kappa_\lambda}i_{iP}^g(z_i, \omega)\right]. \tag{21}$$

Note that we can verify that V_m is continuous, in which case we have $V_{mP}(z_i, \omega) = V_{mD}(z_i, \omega)$, which is consistent with the fact that the electric field is finite. Thus, one sees that when the synaptic current is known at a given position, the spatial profile of V_m can be calculated exactly for a continuous cylinder compartment.

It follows that one can deduce the spatial and frequency profiles of V_m when we know the current generated by each synapse, thanks to the superposition principle. Finally, one can directly calculate the generalized current by applying the following equation:

$$i_i^g = -\frac{1}{\bar{z}_i}\frac{\partial V_m}{\partial z} \tag{22}$$

on Eq. (10) [20]. We obtain the generalized axial current generated by a single synapse:

$$i_{iD}^g(z, \omega) = -\frac{\kappa_\lambda}{\bar{z}_i}\left[A_D^+(z_i, \omega)e^{+\kappa_\lambda z} + A_D^-(z_i, \omega)e^{-\kappa_\lambda z}\right]$$

$$i_{iP}^g(z, \omega) = +\frac{\kappa_\lambda}{\bar{z}_i}\left[A_P^+(z_i, \omega)e^{+\kappa_\lambda(l-z)} - \frac{\kappa_\lambda}{\bar{z}_i}A_P^-(z_i, \omega)e^{-\kappa_\lambda(l-z)}\right]. \tag{23}$$

To obtain the total axial current, one has just to sum up the contributions of each synapse. Note that this "linear" assumption only holds for current-based inputs, and a modified model is needed to account for conductance-based inputs (not shown).

Finally, the knowledge of the generalized axial current permits to determine the boundary conditions on $\vec{B}$ and apply the method developed above [Eq. (7)]. In the next section, we apply this strategy to calculate the magnetic induction in different situations.

B. Simulations of $\vec{B}$ in extracellular space

In this section, we apply the theory to a ball-and-stick type of model of the neuron [21,22], using two different approximations of the extracellular medium and cytoplasm impedance, either when they are purely resistive (Ohmic) or when ionic diffusion is taken into account, resulting in Warburg-type impedances [20].

To do this, we model the ensemble of synaptic current sources as a "stochastic dipole" consisting of two stochastic currents, stemming from excitatory and inhibitory synapses. Each synaptic current is described by a shot noise given by

$$i_s = \sum_{n=1}^{N} cH(t - t_n)e^{-(t-t_n)/\tau_m}, \tag{24}$$

where H is the Heaviside function. The stochastic variable t_n follows a time-independent law. We have chosen $\tau_m = 5$ ms which corresponds to *in vivo* conditions, $c = +1$ nA for excitatory synapses, and $c = -1$ nA for inhibitory synapses (Fig. 6).

In the simulations, we have simulated a ball-and-stick neuron model with a dendrite of 600 μm length and 2 μm constant diameter, and a spherical soma of 7.5 μm radius. The synaptic currents were located at a distance of 57.5 μm of the soma for inhibitory synapses, and respectively 357.5 μm for excitatory synapses. Note that this particular choice was made here to simplify the model. This arrangement generates a dipole which approximates the fact that inhibitory synapses are more dense in the soma or proximal region of the neuron, while excitatory synapses are denser in more distal dendrites [30].

1. Magnetic induction generated by a ball-and-stick model with resistive media

We start by calculating the magnetic induction for the "standard model" where the extracellular medium and cytoplasm are both resistive. The electric conductivity of cytoplasm was of 3 S/m, and that of the extracellular medium was of 5 S/m, in agreement with previous models [17,18,22,23].
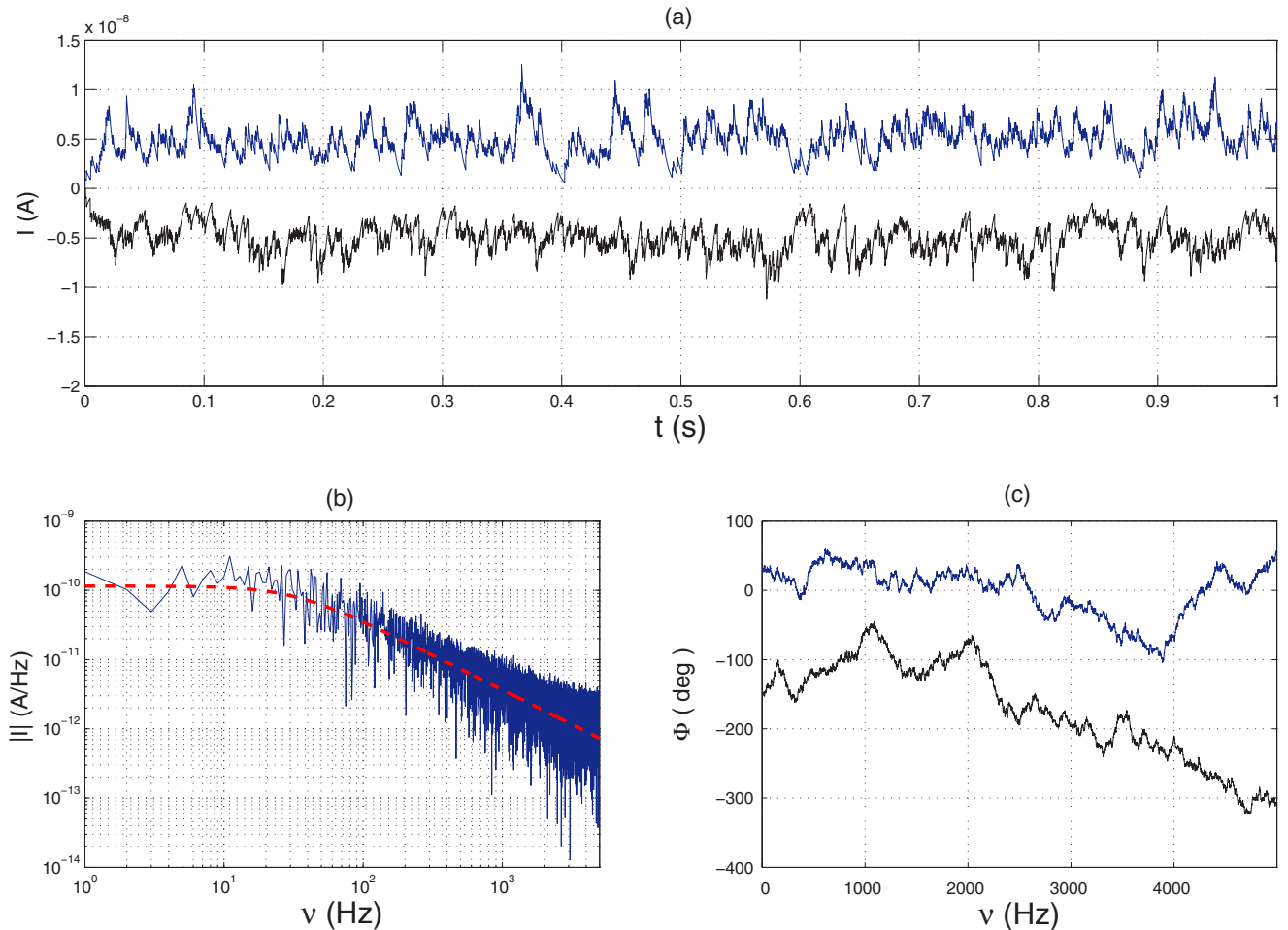
FIG. 6. (Color online) Synaptic current sources used in the simulations. (a) Example of excitatory (blue, top curve) and inhibitory (black, bottom curve) current sources used in simulations. These examples consists of 1000 random synaptic events per second. (b) and (c) Modulus and phase, respectively, of the complex Fourier transform of these processes. Note that the inhibitory current in not represented in (b) because its modulus is identical to that of the excitatory current. The red dashed line in (b) corresponds to a Lorentzian ($\frac{A}{1+i\omega\tau_m}$) with $\tau_m = 5$ ms and $|A| = 1$ nA).

The magnetic induction generated by the resistive model is described in Fig. 7. We can see that, for a given frequency, the modulus of $\mathbf{B}^\theta$ is almost constant in space over the dendritic branch in the region between the two locations of the synaptic currents. It is also smaller outside of this region. Note that the attenuation of $\mathbf{B}^\theta$ is completely different whether excitatory or inhibitory synapses are present (Fig. 7, blue dashed curves). Finally, we also see that the attenuation of the axial current is very close to a linear law, although in reality we have a linear combination of exponentials [see Eq. (24)].

The frequency dependence of $\mathbf{B}^\theta$ is shown in Fig. 8 for the resistive model. The frequency dependence depends on the position on the dendrite. Between the two synapse sites (black curves), the frequency dependence does not depend on the position, and the scaling exponent is close to -1.5. However, the phase of $\mathbf{B}^\theta$ is position dependent, but is very small (between 0 and -3 degrees). In this region, the frequency scaling begins at frequencies larger than about 10 Hz.

In the "proximal" region, between the soma and the location of inhibitory synapses, the frequency dependence is different according to the exact position on the dendrite (Fig. 8, red

curves) and the frequency scaling occurs at frequencies larger than 1000 Hz. However, the frequency scaling is almost identical, and the exponent is about -1. The contribution of this region to the value of $\mathbf{B}^\theta$ can be negligible compared to the preceding region for the frequency range considered here (<1000 Hz). The phase also shows little variations and is of small amplitude (between 1 and 3 degrees).

Finally, for the "distal" region, away of the site of excitatory synapses, the frequency dependence of the modulus of $\mathbf{B}^\theta$ varies with the position on the dendrite and is significant only from about 1000 Hz, similar to the proximal region. The dependencies are almost identical between proximal and distal regions, except for frequencies larger than 1000 Hz. Note that the contribution of these two regions to the value of $\mathbf{B}^\theta$ is very small and can be considered negligible compared to the region between the two synaptic sites (for frequencies smaller than 1000 Hz). The Fourier phase shows little variations between 1 and 5000 Hz. The frequency scaling exponent is of the order of -1.5 between 2000 and 4000 Hz. Note that the numerical simulations also indicate that the boundary conditions on the stick are very sensitive to the cytoplasm resistance but are less sensitive to the extracellular resistance.
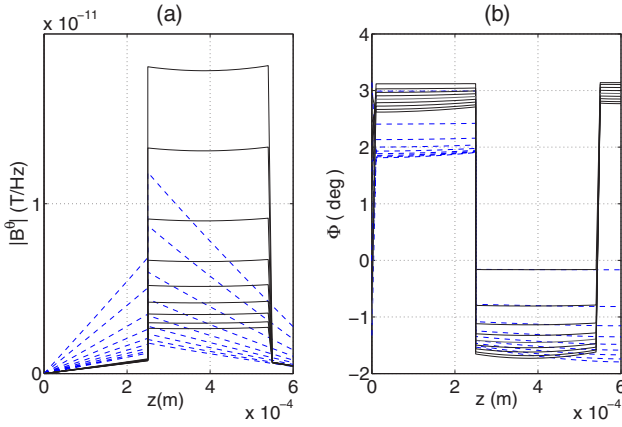
FIG. 7. (Color online) Magnetic induction for the resistive model. $\mathbf{B}^\theta$ is shown here at the surface of the dendrite, as a function of position (distance to soma) for different frequencies between 1 Hz and 5000 Hz. The blue dashed lines correspond to $\mathbf{B}^\theta$ generated when only excitatory synapses were present, and the black curves correspond to both synapses present. $\mathbf{B}^\theta$ is always decreasing with frequency and is larger and approximately constant between the two locations of the synaptic currents.

2. Magnetic induction generated by a ball-and-stick model with diffusive media

We now illustrate the same example as above, but when the intracellular (cytoplasm) and extracellular media are described by a diffusive-type Warburg impedance (Figs. 9 and 10). We have assumed that the cytoplasm admittance is $\gamma = 3\frac{\sqrt{\omega}(1+i)}{\sqrt{2}}$ S/m, while that of the extracellular medium is $5\frac{\sqrt{\omega}(1+i)}{\sqrt{2}}$ S/m. These values were chosen such that the modulus of the admittance is the same as the preceding example with resistive media (see Sec. III B 1) for $\omega = 1$ Hz.
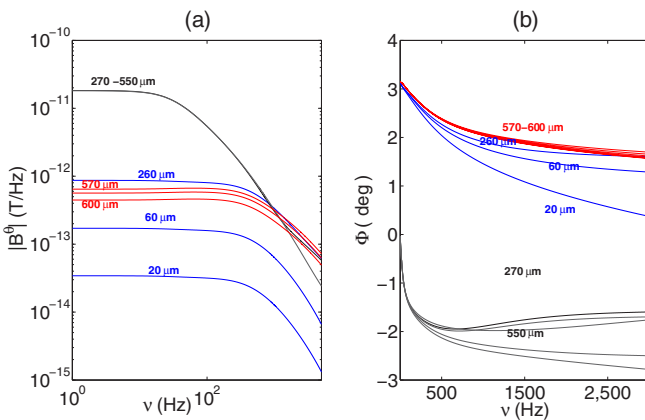

FIG. 9. (Color online) Magnetic induction $\mathbf{B}^\theta$ on the surface of the dendrite for a neuron embedded in diffusive media. $\mathbf{B}^\theta$ is represented for different frequencies. The blue dashed curves correspond to $\mathbf{B}^\theta$ produced at the surface of the dendrite with only excitatory synapses, and black curves correspond to excitatory and inhibitory synapses present. We see that $\mathbf{B}^\theta$ is a decreasing function of frequency and is higher towards inhibitory synapses, and low outside of this region.

When calculating the magnetic induction, we see that the modulus of $\mathbf{B}^\theta$ on the dendrite surface increases when one approaches the position of inhibitory synapses, but is very small outside of this region (Fig. 9, black curves). Note that the attenuation law of $\mathbf{B}^\theta$ along the dendritic branch is completely different from that with only excitatory synapses present (Fig. 9, blue dashed curves). We also see that the attenuation of the axial current is very close to a straight line, but in reality it is given by a sum of exponentials [see Eqs. (24)].

FIG. 8. (Color online) Frequency profile of the magnetic field for the resistive model. $\mathbf{B}^\theta$ at the surface of the dendrite is represented as a function of frequency at different positions (both excitatory and inhibitory synapses were present). The red curves correspond to different positions between the inhibitory synapses and the soma, the blue curves are taken at different positions between the excitatory synapses and the end of the dendrite, and the black curves represent positions in between the two synapse sites. Note that the modulus of $\mathbf{B}^\theta$ does not depend on position.
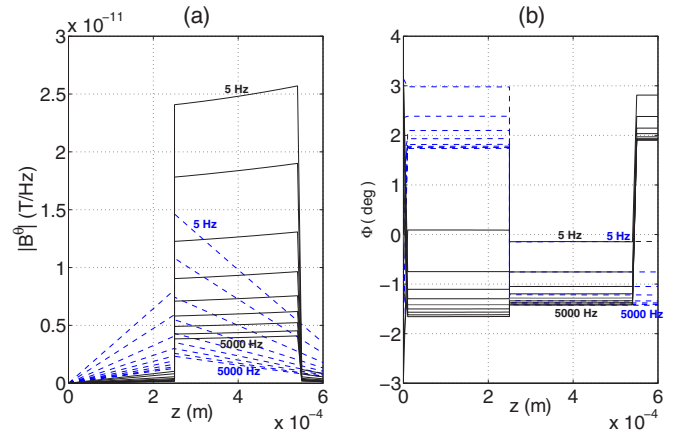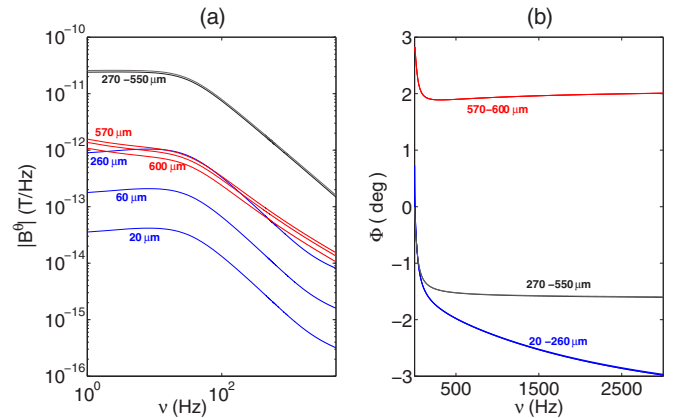

FIG. 10. (Color online) Magnetic induction $\mathbf{B}^\theta$ on the surface of the dendrite, as a function of frequency, for a neuron within diffusive media. $\mathbf{B}^\theta$ is represented for different positions on the dendrite, with both excitatory and inhibitory synapses present. One can see three distinct regions: proximal region between the soma and the location of inhibitory synapses (red curves), region between the two synaptic sites (black curves), and the distal region between the location of excitatory synapses and the end of the dendrite (blue curves). Note that the modulus of $\mathbf{B}^\theta$ depends very weakly on dendritic position when we are in between the two synaptic sites.

We can also see that the frequency dependence of $\mathbf{B}^\theta$ depends on the region considered in the dendrite (Fig. 10). Between the two synaptic sites (black curves in Fig. 10), the frequency dependence is almost independent of position, with a scaling exponent close to -1 (in the resistive case, it was -1.5 for the same conditions; see Fig. 8). The Fourier phase of $\mathbf{B}^\theta$ displays little variation. The frequency dependence begins at a frequency around 30 Hz.

In the "proximal" region, from the soma to the beginning of the dendrite, the frequency dependence of the modulus of $\mathbf{B}^\theta$ depends on position and is present at all frequency bands. Between 1 and 10 Hz, the scaling exponent is close to $1/4$, which would imply a PSD proportional to $1/f^{1/2}$. This result is very different from the resistive case, which had a negligible dependence at those frequencies (see Fig. 8). Note that the contribution of this region to the value of $\mathbf{B}^\theta$ can be considered negligible compared to the preceding region, for all frequencies between 1 and 5000 Hz (which was not the case for resistive media; see Fig. 8). Finally, the Fourier phase is positive and approximately constant for those frequencies. The scaling exponent is -0.5 between 2000 and 4000 Hz, while it was -1 in the resistive case examined above.

Finally, for the "distal" region, at the end of the dendrite, the frequency dependence of the modulus of $\mathbf{B}^\theta$ varies with position, and we observe a resonance around 30 Hz (Fig. 10). A similar resonance was also seen previously in the cable equation for diffusive media [20]. Similar to the proximal region, the contribution of the distal region to the value of $\mathbf{B}^\theta$ is very weak (for frequencies lower than 1000 Hz). The Fourier phase shows little variations. The scaling exponent is around -1 between 2000 and 4000 Hz, similarly to the region between the synaptic sites. As above, the boundary conditions of the surface of the "stick" are much more sensitive to the cytoplasm impedance.

3. Attenuation law with distance in extracellular space

In this section we show that the attenuation law of B^θ relative to distance in the extracellular medium (Figs. 11 and 12) depends on the nature of the extracellular impedance. Figure 11 shows an example of the attenuation obtained in a resistive medium, while Fig. 12 shows the same for a medium with diffusive properties (Warburg impedance). The parameters are the same as for Figs. 7–8 and Figs. 9–10, respectively.

From Figs. 11 and 12, one can see that the nature of the extracellular medium has little effect on the attenuation law relative to distance r for a position z in between the synaptic sites. However, the nature of the medium is more influential outside of this region. For $r < 100\ \mu m = l/6$, the attenuation varies as $1/r$ and is dependent on frequency, while for $r > 200\ \mu m = l/3$, the attenuation varies as $1/r^2$. The nature of the medium changes the position dependence of the magnetic induction. In a diffusive medium, the "return current" more strongly depends on frequency compared to a resistive medium, and the partial derivative of $\mathbf{B}^\theta$ relative to z is less abrupt (low-pass filter).

When comparing Figures 7 to 12, one can see that the nature of the cytoplasm impedance has a larger effect than the extracellular impedance. The intracellular impedance has more effect on the slope of the frequency dependence of the magnetic induction on the surface of the neuron (boundary conditions), while the extracellular impedance affects more the attenuation law with distance. The latter effect is due to the fact that the extracellular impedance affects the return currents, and therefore plays a screening effect on $\mathbf{B}^\theta$, in a frequency-dependent manner. It is interesting to see that the nature of the impedances affects $\mathbf{B}^\theta$, although we have roughly the same magnetic permeability as a vacuum.

IV. DISCUSSION

In this paper, we have derived a cable formalism to calculate the extracellular magnetic induction $\vec{\mathbf{B}}$ generated by neuronal structures. A contribution of this formalism is to allow us to evaluate $\vec{\mathbf{B}}$ in neurons embedded in media which can have arbitrary complex electrical properties, such as, for example, taking into account diffusive or capacitive effects in the extracellular space. To this end, it is necessary to use the "generalized cable" formalism introduced recently [20], which generalizes the classic Rall cable formalism [17,18] but for neurons embedded in media with complex electrical properties. Using this generalized cable, it was shown that the nature of the medium influences many properties such as voltage and axial current attenuation [20]. We show here that it can also influence neuronal magnetic fields.

To compare with previous approaches, it is important to note that the present formalism is based on a multiscale mean-field theory. We consider the neuron in interaction with the "mean" extracellular medium, characterized by a specific impedance [20]. Using such a formalism, we can study the influence of the nature of the extracellular medium impedance on the axial current and deduce its effect on the spatial and frequency profile of $\vec{\mathbf{B}}$. This represents a net advantage over a classical mean-field theory, where the medium is considered as a continuum where the biological sources are not explicitly represented. An alternative approach consists of using the Biot-Savart law in three dimensions, within a mean-field model of the cortex [2]. This approach can be considered as a first-order approximation of the formalism we present here. However, it is strictly limited to resistive media, and cannot be used to investigate the fields generated in nonresistive or nonhomogeneous media, with complex electrical properties. In such a case, the present formalism should be used.

The present formalism can be extended or further developed in several ways. First, some predictions of the formalism can be tested experimentally. Our numerical simulations show that the electric nature of intracellular and extracellular media influence many properties of $\vec{\mathbf{B}}$. This result may seem surprising at first sight, because the magnetic field itself is not filtered by the medium, so we would expect $\vec{\mathbf{B}}$ to be independent of the electrical properties of extracellular space. However, as mentioned above, these properties influence the membrane currents and the axial currents in the neuron, and thus, in turn, they also influence $\vec{\mathbf{B}}$. So this property constitutes an important prediction of the present formalism: the nature of the extracellular medium should affect the frequency dependence of $\vec{\mathbf{B}}$, which can be measured experimentally. For example, according to the present work, the PSD of $\vec{\mathbf{B}}$ should present
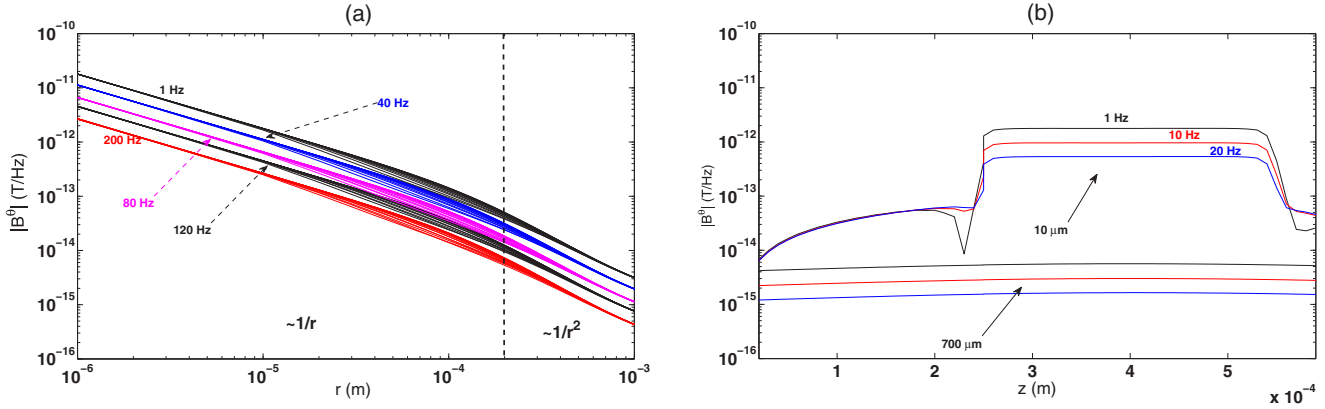
FIG. 11. (Color online) Distance dependence of the magnetic induction for a ball-and-stick model with resistive media. The boundary conditions are represented in Figs. 10 and 11. (a) Attenuation law for the modulus of $\mathbf{B}^\theta$ relative to r (direction perpendicular to the axis of the stick). For $r < 100\ \mu$m $= l/6$, the attenuation is varying as $1/r$ with a proportionality constant that depends on frequency. For $r > 200\ \mu$m $= l/3$, the attenuation varies as $1/r^2$ and is roughly independent of frequency. (b) Attenuation law relative to z (direction parallel to the axis of the stick). The attenuation does not depend on frequency for positions outside the regions between the synapses. In all cases, the phase varied very little and was not represented.

a frequency scaling which reflects the frequency scaling of the impedances of the intracellular and extracellular media. This influence may perhaps explain the particular frequency scaling observed for MEG signals [14] (reviewed in Ref. [7]). The fact that the extracellular impedance influences $\vec{\mathbf{B}}$ also has clear consequences for the so-called inverse problem of finding the neuronal sources from recorded electric or magnetic brain signals. These types of analysis constitute an important future development of the present work.

A second possible direction for future work is to extend the present formalism to simulate complex neuronal morphologies. We have shown here that $\vec{\mathbf{B}}$ can be approximated by successive analytical iterations. Such an analytic approach relies on the assumption that the continuous cylinder is of constant diameter, but it is valid for arbitrarily complex extracellular electric properties. Thus, it should be possible to apply the same approach to simulate any complex neuronal morphology, using a set of such continuous cylinder compartments. Because the approximate solution is analytic, this formalism can lead

to very efficient algorithms to simulate the magnetic field generated by complex neuronal morphologies or populations of neurons. This also constitutes a main follow-up of the present work.

It is important to note that some of the previously-proposed models of magnetic fields generated by complex neuronal morphologies are based on a direct application of the Biot-Savart law [5,31], which neglects the return currents and is equivalent to consider that the neuron is embedded into vacuum. In reality, the neuron exchanges currents with extracellular space, and generates return currents, which also participate to the the genesis of $\vec{\mathbf{B}}$. One main advantage of the present formalism is that these return currents are taken into account, and thus we believe that it provides a good estimate of the "net" magnetic induction $\vec{\mathbf{B}}$ generated by neurons embedded in realistic extracellular media.

A third possible extension of the present formalism is to include the effect of magnetic stimulation. Because of the recent emergence of noninvasive techniques such as
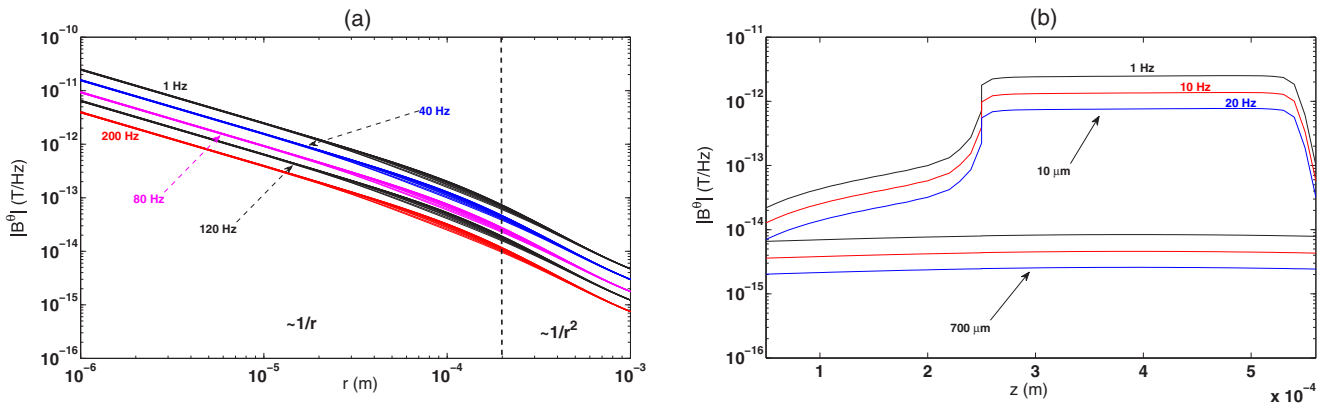

FIG. 12. (Color online) Distance dependence of the magnetic induction for a ball-and-stick model with diffusive media. The same arrangement as in Fig. 11, but with boundary conditions as represented in Figs. 9 and 10. (a) Attenuation law for the modulus of $\mathbf{B}^\theta$ relative to r. As for the resistive model, the attenuation varies as $1/r$ for $r < 100\ \mu$m $= l/6$, and as $1/r^2$ for $r > 200\ \mu$m $= l/3$. (b) Attenuation law relative to z. Contrary to the resistive model, the attenuation depends on frequency for all positions.

the transcranial magnetic stimulation [28], it is likely that understanding the effect of magnetic stimulation will become increasingly important in the future. In our formalism, it is possible to integrate this effect from the right-hand term of Eq. (9), because this term takes into account the phenomenon of electromagnetic induction. Evidently, the solution in space will be different from what is presented here, because this additional term implies $\nabla^2 \vec{\mathbf{B}} \neq 0$. However, most of the formalism developed here can be used because we have $\vec{E} = -\vec{\nabla} V - \frac{\partial \vec{A}}{\partial t}$ instead of $\vec{E} = -\vec{\nabla} V$. Thus, with minor modifications, it is possible to consider the effect of magnetic stimulation in neurons, together with the complex properties of the extracellular medium, generalizing previous approaches [32]. Here again, the effect of magnetic stimulation depends on the admittance of the medium, which constitutes another way by which neuronal behavior may depend on the electric properties of extracellular space.

APPENDIX A: CYLINDRIC SYMMETRY AND THE DIRECTION OF $\vec{B}$

In this Appendix, we calculate the direction of $\vec{B}$. To do this, we use the expression of the vector potential $\vec{\mathbf{A}}$ ($\vec{\mathbf{B}} = \vec{\nabla} \times \vec{\mathbf{A}}$) in conditions of Coulomb's gauge ($\vec{\nabla} \cdot \vec{\mathbf{A}} = 0$) and the Kelvin-Maxwell law ($\vec{\nabla} \cdot \vec{\mathbf{B}} = 0$ [Eq. 1(iii)]).

1. Component $\mathbf{B}^z$ on the surface of the continuous cylinder compartment

If one substitutes in Eq. 1(iv), $\vec{\mathbf{B}} = \vec{\nabla} \times \vec{\mathbf{A}}$ (within Coulomb's gauge), we obtain

$$\vec{\nabla} \times \vec{\mathbf{B}} = \vec{\nabla} \times (\vec{\nabla} \times \vec{\mathbf{A}})$$
$$\equiv -\nabla^2 \vec{\mathbf{A}} + \vec{\nabla}(\vec{\nabla} \cdot \vec{\mathbf{A}}) = -\nabla^2 \vec{\mathbf{A}} = \mu_o \vec{\mathbf{j}}^g. \quad (A1)$$

Thus, each component of $\vec{\mathbf{A}}$ is solution of a "Poisson"-type equation, and we can write in cylindric coordinates:

$$\vec{\mathbf{A}}(\vec{x}, \omega)$$
$$= \frac{\mu_o}{4\pi} \iiint_{\mathcal{E}_t} \frac{\vec{\mathbf{j}}^g(\vec{x}', \omega)}{\sqrt{r^2 + r'^2 + 2rr' \cos(\theta - \theta') + (z - z')^2}}$$
$$\times r' dr' d\theta' dz' \quad (A2)$$

if we assume that $\vec{\mathbf{A}} = 0$ at infinite distance. The integration domain $\mathcal{E}_t$ represents all space. However, assuming that the current field in a continuous cylinder compartment follows cylindric symmetry, we can write that in any point of space, the generalized current density is given by $\vec{\mathbf{j}}^g = \mathbf{j}^{rg}(r, z)\hat{e}_r + \mathbf{j}^{zg}(r, z)\hat{e}_z$ where $\hat{e}_z$ and $\hat{e}_r$ are, respectively, parallel and perpendicular to the symmetry axis of the axial current. It follows that the vector potential is of the form $\vec{\mathbf{A}} = \mathbf{A}^r(r, z)\hat{e}_r + \mathbf{A}^z(r, z)\hat{e}_z$

[Eq. (A2)]. Thus, the component $\mathbf{B}^z$ of $\vec{\mathbf{B}}$ is always equal to zero, since we have $\mathbf{B}^z = (\vec{\nabla} \times \vec{\mathbf{A}})^z = 0$.

2. The component $\mathbf{B}^r$ on the surface of the continuous cylinder compartment

The application of Kelvin-Maxwell's law [Eq. 1(iii)] implies that the surface integral (Fig. 2) of $\mathbf{B}^r$ gives

$$\iint_{\mathcal{S}_B} \mathbf{B}^r \, dS = \iint_{\partial \mathcal{D}} \vec{\mathbf{B}} \cdot \hat{n} \, dS \equiv \iiint_{\mathcal{D}} \vec{\nabla} \cdot \vec{\mathbf{B}} \, dv = 0 \quad (A3)$$

because the component $\mathbf{B}^z = 0 \Rightarrow \iint_{\mathcal{S}_A} \vec{\mathbf{B}} \cdot \hat{n} \, dS = \iint_{\mathcal{S}_C} \vec{\mathbf{B}} \cdot \hat{n} \, dS = \iint_{\mathcal{S}_A} |\mathbf{B}^z| \, dS = \iint_{\mathcal{S}_C} |\mathbf{B}^z| \, dS = 0$ (for a plane perpendicular to the surface $\mathcal{S}_B$ of the compartment. Thus, we can deduce that $\mathbf{B}^r = 0$ because the integral of $\mathbf{B}^r$ is zero for a surface of arbitrary length $\mathcal{S}_B$. Consequently, the general expression of $\vec{\mathbf{B}}$ over the surface of a continuous cylinder compartment is given by

$$\vec{\mathbf{B}} = \mathbf{B}^\theta \hat{e}_\theta. \quad (A4)$$

Note that electromagnetic induction is taken into account in this derivation because we did not use the explicit value of $\vec{\nabla} \times \vec{\mathbf{E}}$ when deriving Eq. 1(ii).

APPENDIX B: SOLVING $\nabla^2 \vec{\mathbf{B}} = 0$ FOR A CONTINUOUS CYLINDER COMPARTMENT

In this Appendix, we introduce an iterative method to calculate the solution of $\nabla^2 \vec{\mathbf{B}} = 0$ for a continuous cylinder compartment of radius a and length l, when the values of $\mathbf{B}^\theta$ at its surface are known. We approach the solution analytically by using the mathematical relations between the different currents present in the neuron and the magnetic induction that these currents produce.

We calculate $\mathbf{B}^\theta$ in space assuming that Region P contains only one continuous cylinder compartment [Fig. 13(a)], but the method can be easily generalized to the case with several compartments [Fig. 13(b)]. In this case, to generalize to N_p compartments, one must determine the boundary conditions of $\mathbf{B}^\theta$ for each compartment inside Region P. In all cases, we assume that $\mathbf{B}^\theta$ satisfies (1) $\mathbf{B}^\theta$ is a continuous function on the borders L-P and P-R (Fig. 13); (2) $\mathbf{B}^\theta = 0$ at infinite distance; and (3) $\mathbf{B}^\theta = 0$ on the symmetry axis of the compartment.

To calculate the solution, we extend the original compartment in Regions L and R using the same radius a [Fig. 13(a)]. Note that by convention, we place the symmetry axis on the z axis, and place the continuous cylinder between coordinates $z = 0$ and $z = l > 0$.

At the first order of the iteration, we assume that

$$\mathbf{B}^\theta(\mathbf{a}, \mathbf{z} < \mathbf{0}, \omega) = \mathbf{0} \quad \mathbf{B}^\theta(\mathbf{a}, \mathbf{z} > \mathbf{l}, \omega) = \mathbf{0}.$$

over the surfaces of the extended compartment (L and R), which ensures the spatial continuity of the first-order solution at the border L-P. *A priori* this choice is arbitrary, but we have chosen here a particular attenuation law which neglects the radius of the extended compartment. Following this first choice, we calculate the solution of Eq. (9) by using the
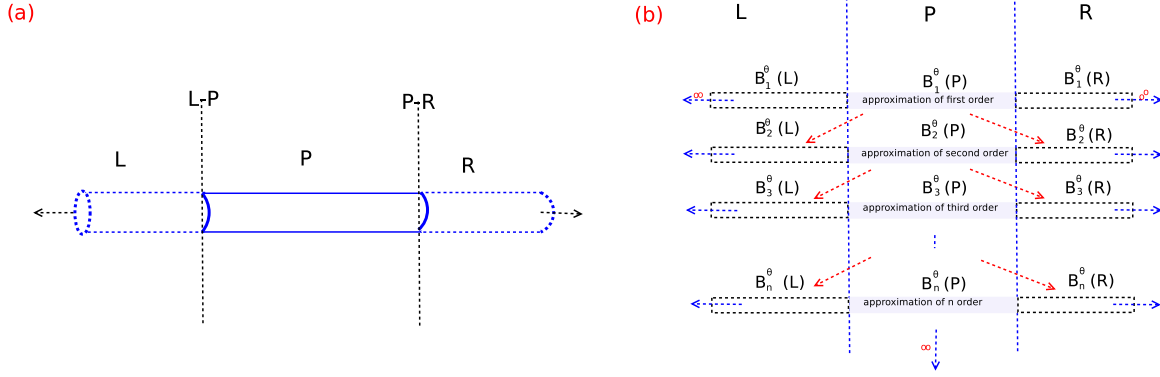
(a)

(b)

FIG. 13. (Color online) Scheme to calculate $\mathbf{B}^\theta$. (a) Extension of the compartment in Regions L and R when the principal region (P) consists of a single cylinder compartment of radius a. (b) Calculation scheme. In a first step, we calculate in Fourier space the field $\mathbf{B}^\theta$ by assuming that the boundary conditions on the cylinder are such that $\mathbf{B}^\theta(a, z < 0, \omega) = 0$ and $\mathbf{B}^\theta(a, z > l, \omega) = 0$ in Regions L and R. The solution of $\nabla^2 \vec{\mathbf{B}} = 0$ obtained in such conditions is called the *first-order solution* of $\mathbf{B}^\theta$. In a second step, we improve the boundary conditions by applying the Hankel transform of order 1 relative to r, and the continuity principle of the solution at the borders L-P and P-R. We reevaluate the solution of $\nabla^2 \vec{\mathbf{B}} = 0$ with these new boundary conditions to obtain a *second-order solution* of $\mathbf{B}^\theta$. The same iteration is continued.

complex Fourier transform along z. This leads to

$$\mathbf{B}^\theta(r, z, \omega) = \frac{1}{2\pi} \int_{-\infty}^{+\infty} g(r, k_z, \omega) e^{+ik_z z}\, dk_Z, \quad (\text{B1})$$

where

$$g(r, k_z, \omega) = \int_{-\infty}^{+\infty} \mathbf{B}^\theta(r, z, \omega) e^{-ik_z z}\, dz. \quad (\text{B2})$$

We next substitute Eq. (B1) in Eq. (9), which leads to

$$\int_{-\infty}^{+\infty} \left[\frac{d^2 g}{dr^2} + \frac{1}{r}\frac{dg}{dr} - \left(k_z^2 + \frac{1}{r^2} \right) g \right] e^{+ik_z z}\, dz = 0. \quad (\text{B3})$$

when electromagnetic induction is neglected.

Thus, we have (for k_z and ω fixed) the following equality:

$$\frac{d^2 g}{dr^2} + \frac{1}{r}\frac{dg}{dr} - \left(k_z^2 + \frac{1}{r^2} \right) g = 0 \quad (\text{B4})$$

because the Fourier transform of zero is zero. It follows that the function g must be solution of the modified Bessel differential equation of order 1. The general solution of such an equation is given by

$$g(r, k_z, \omega) = c(k_z, \omega) I_1(|k_z| r) + d(k_z, \omega) K_1(|k_z| r), \quad (\text{B5})$$

where I_1 is a a modified Bessel function of first kind of order 1 and K_1 is a modified Bessel function of second kind of order 1.[9] Such functions are illustrated in Fig. 14 as a function of r for typical parameter values that correspond to neurons. Note that we must assume that k_z is very small for function $K_1(|k_z| r)$ to have a significant value for large r. For a fixed value of K_1, we have $k_z \sim 1/r$. Note that, for the typical geometrical size of neurons and distances studied here (< 1 mm), the values of k_r are pertinent when they are larger than 1000 m^{-1} (Fig. 15).

Finally, to evaluate the coefficients $c(k_z, \omega)$ and $d(k_z, \omega)$, we apply the continuity condition of $\mathbf{B}^\theta$ between the interior and exterior of the extended compartment, and that $\mathbf{B}^\theta$ must be zero on the symmetry axis of the compartment ($r = 0$), as well as at infinite distance. Because $|I_1(\infty, \omega)| = \infty$, we must assume that $c(k_z, \omega) = 0$ outside of the cylinder, and because $|K_1(0, \omega)| = \infty$, we must assume that $d(k_z, \omega) = 0$ inside of the cylinder. Taking these conditions into account, we obtain

$$\text{exterior } r \geqslant a \; d(k_z, \omega) = \frac{g(a, k_z, \omega)}{K_1(|k_z| a)}$$

$$\text{interior } r \leqslant a \; c(k_z, \omega) = \frac{g(a, k_z, \omega)}{I_1(|k_z| a)} \quad (\text{B6})$$

It follows that the approximative solution of first-order is given by

$$\text{exterior } r \geqslant a \; \mathbf{B}^\theta(r, z, \omega)$$
$$= \frac{1}{2\pi} \int_{-\infty}^{+\infty} g(a, k_z, \omega) \frac{K_1(|k_z| r)}{K_1(|k_z| a)} e^{+ik_z z}\, dk_z$$

$$\text{interior } r \leqslant a \; \mathbf{B}^\theta(r, z, \omega)$$
$$= \frac{1}{2\pi} \int_{-\infty}^{+\infty} g(a, k_z, \omega) \frac{I_1(|k_z| r)}{I_1(|k_z| a)} e^{+ik_z z}\, dk_z, \quad (\text{B7})$$

where the function $g(a, k_z, \omega)$ is given by Eq. (B2):

$$g(a, k_z, \omega) = \int_{-\infty}^{+\infty} \mathbf{B}^\theta(a, z, \omega) e^{-ik_z z}\, dz. \quad (\text{B8})$$

This first iteration gives us a first-order approximation of $\mathbf{B}^\theta$, which is refined in successive iterations, as schematized in Fig. 13(b). We use the first-order approximation in Region P to calculate the solutions in Regions L and R. To do this, we use the first-order Hankel transform[10] for the variable r. To

---

[9] We have $J_1(ir') = i I_1(r')$ and $Y_1(ir') = I_1(r') + \frac{2}{\pi} i K_1(r')$, where J_1 is the modified Bessel function of first kind of order 1, and Y_1 is the Bessel function of second kind of order 1.

[10] This is equivalent to the first-order Fourier-Bessel transform. This particular transform was chosen here because the function $J_1(k_r r)$ has the same boundary conditions as in the present problem [Figs. 14(c)–14(d)]: it is equal to zero for $r = 0$ and for $r \to \infty$.
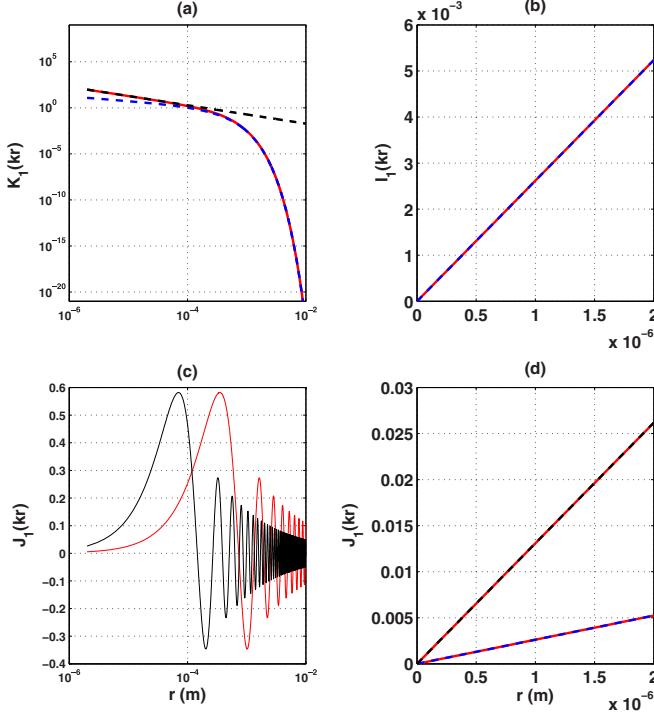
FIG. 14. (Color online) Bessel functions for a continuous cylinder compartment. The Bessel functions are indicated as a function of the distance r perpendicular to the axis of the cylinder; the cylinder had a length l of 300 μm and a radius $a = 2$ μm. We have $k' = 2 \times 10^4$ m^{-1}. (a) K_1 as a function of distance. The red curve shows the function $K_1(kr)$ with $k = k'$. The black dashed straight line represents the function $1/kr$, and the blue dashed curve represents the asymptotic behavior of K_1 for $r \to \infty$. We have $K_1(kr) \xrightarrow{\infty} \sqrt{\frac{\pi}{2kr}} e^{-kr}$. At short distances (smaller than $2/k$), the function K_1 decays linearly with distance, but for large distances ($r > \pi/k$), it converges more rapidly than an exponential decay with distance. (b) The function I_1 (modified Bessel function of first kind of order 1) is well approximated by a straight line [$I_1(kr) = kr/2$] for $k = k'$ when $r < a$. (c) Bessel function of first kind of order 1 when $r > a$. The blue and black curves correspond, respectively, to $k = k'$ and $k = 5k'$. Note that we have $J_1(kr) \xrightarrow{\infty} \sqrt{\frac{2}{\pi kr}} \cos(kr - \frac{3\pi}{4})$. We see that when k is large enough, the function $J_1(kr)$ can capture small spatial variations. (d) The Bessel function of first kind of order 1 is equivalent to a straight line [$J_1(kr) = kr/2$] when $r < a$. The blue dashed curve corresponds to approximating $J_1(kr)$ by a linear law for $k = k'$, while the black dashed curve is the linear approximation for $k = 5k'$. The red curves correspond to $J_1(kr)$ for $k = k'$ and $k = 5k'$ [33,34].

do this, one applies the continuity principle at the borders L-P and P-R. This gives the following relations:

$$\mathbf{B}^\theta(r,z,\omega) = \int_0^\infty k_r h_1(k_r,z,\omega) J_1(k_r r)\, dk_r \quad \text{(B9)}$$

where

$$h_1(k_r,z,\omega) = \int_0^\infty r\mathbf{B}^\theta(r,z,\omega) J_1(k_r r)\, dr \quad \text{(B10)}$$

in Regions L and R.

The Hankel transform is a calculus technique similar to the wavelet transform [Figs. 14(c)–14(d)]. Note that the values of k_r vary inversely proportional to the values of r, similarly to the relation between parameter k_z and z above (Fig. 15).

By substituting Eq. (B9) into Eq. (9), and neglecting electromagnetic induction as above, we obtain for fixed ω:

$$\int_0^\infty \left\{ \left[r^2 \frac{d^2 J_1(k_r r)}{dr^2} + r\frac{d J_1(k_r r)}{dr} - J_1(k_r r) \right] \right.$$
$$\left. \times h_1(k_r,z,\omega) + r^2 \frac{d^2 h_1(k_r,z,\omega)}{dz^2} \right\} k_r\, dk_r = 0. \quad \text{(B11)}$$

In addition, the first-order Bessel function satisfies the following equation:

$$r^2 \frac{d^2 J_1(k_r r)}{dr^2} + r\frac{d J_1(k_r r)}{dr} + \left[k_r^2 r^2 - 1 \right] J_1(k_r r) = 0. \quad \text{(B12)}$$

It follows that

$$\int_0^\infty r^2 \left[\frac{d^2 h_1(k_r,z,\omega)}{dz^2} - k_r^2 h_1(k_r,z,\omega) \right] J_1(k_r r) k_r\, dk_r = 0. \quad \text{(B13)}$$

Because the Hankel transform of zero is zero, we can write for fixed values of k_r and ω:

$$\frac{d^2 h_1}{dz^2} - k_r^2 h_1 = 0. \quad \text{(B14)}$$

Thus, the general solution of Eq. (B14) is given by

$$h_1(k_r,z,\omega) = a(k_r,\omega)e^{+k_r z} + b(k_r,\omega)e^{-k_r z}$$
$$+ c(k_r,\omega)k_r z + d(k_r,\omega). \quad \text{(B15)}$$

Using the condition that $\mathbf{B}^\theta$ vanishes at infinite distance for each frequency implies that, for each frequency, $a = c = d = 0$ when $z > l$, and $a = b = d = 0$ when $z < 0$. Consequently, the solution in Regions L and R are given by

$$\mathbf{B}^\theta(\mathbf{r},\mathbf{z},\omega) = \int_0^\infty h_1^L(k_r,\omega) J_1(k_r r) k e^{-k_r |z|}\, dk_r \, z < 0$$

$$\mathbf{B}^\theta(r,z,\omega) = \int_0^\infty h_1^R(k_r,\omega) J_1(k_r r) k e^{-k_r |z-l|}\, dk_r \, z > l,$$
$$\text{(B16)}$$

where h_1^i for $i = L$ and $i = R$ are given by the continuity conditions at $z = 0$ and $z = l$, and we obtain

$$h_1^L(k_r,\omega) = h_1(k_r,0,\omega) = \int_0^\infty r\mathbf{B}^\theta(r,0,\omega) J_1(k_r r)\, dr$$

$$h_1^R(k_r,\omega) = h_1(k_r,l,\omega) = \int_0^\infty r\mathbf{B}^\theta(r,l,\omega) J_1(k_r r)\, dr.$$
$$\text{(B17)}$$

It follows that we can calculate the new limit conditions on the extended compartment, by applying Eqs. (B1). We obtain

$$\mathbf{B}^\theta(\mathbf{a},\mathbf{z},\omega) = \int_0^\infty h_1^L(k_r,\omega) J_1(k_r a) k e^{-k_r |z|}\, dk_r \, z < 0$$

$$\mathbf{B}^\theta(a,z,\omega) = \int_0^\infty h_1^R(k_r,\omega) J_1(k_r a) k e^{-k_r |z-l|}\, dk_r \, z > l.$$
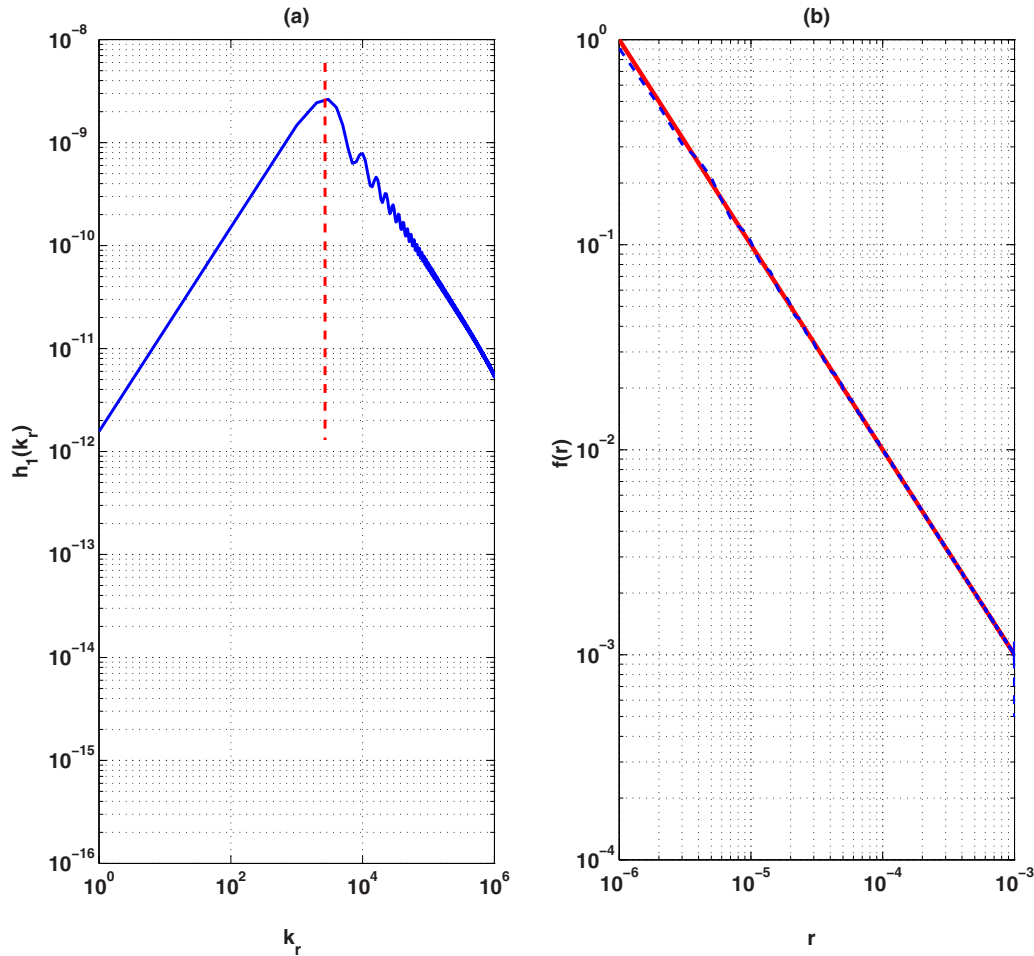$$\text{(B18)}$$

FIG. 15. (Color online) Example of application of the Hankel transform of order 1. (a) Approximation using the Hankel transform of order 1 of the function $f(r) = H(r-a)1/r$ with $a = 1$ μm, $1 < k_r < 5 \times 10^6$, and $\Delta k_r = 10^3$. The values smaller than 10^3 are not significant because of the value of Δk_r is larger than 1000. We can see that the approximation using the Hankel transform is valid for distances up to 1 mm. (b) Inverse transform applied to this approximation (in blue), and comparison with the original function (in red), between 1 μm and 1 mm. The parameter k_r of the Hankel transform plays a similar role as the wave number $(\frac{2\pi}{\lambda})$ in spatial Fourier transform. The larger k_r, the more sensitive to fine spatial details.

After applying the Hankel transform of first order, if we recover the same boundary conditions that were assumed at the borders of the cylinder compartment, then we have reached the exact solution. If this is not the case, we can continue to improve the approximation of the solution by further iterations (Fig. 13). To do this, one considers the original boundary conditions in Region P together with the new expressions for the boundary conditions at the extended compartment (L and R) according to Eqs. (B18). One applies the complex Fourier transform on axis z [Eqs. (B7) and (B8)] to obtain a higher-order approximation. The iteration is then continued until one obtains a satisfactory solution (Fig. 16).

APPENDIX C: CONVERGENCE OF THE ITERATIVE METHOD

In this Appendix, we show that the iterative method of Appendix B converges to a unique solution. We show that the series of successive approximations of $\mathbf{B}^\theta$ increase monotonically and are bounded, which is sufficient to prove convergence.

At every cycle of the iteration, the Laplace equation is solved, which gives a approximation of for $\mathbf{B}^\theta$. By virtue
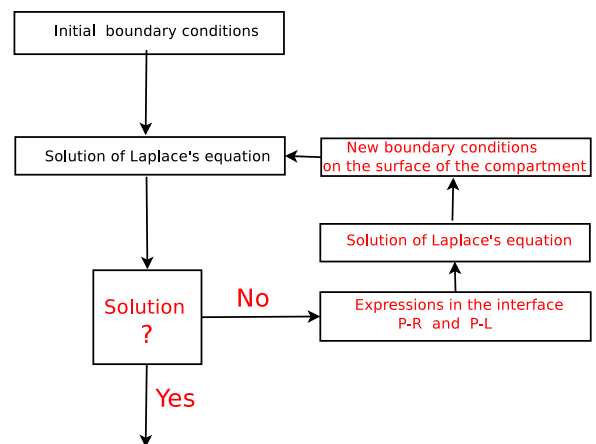

FIG. 16. (Color online) Organigram of the iterative method to calculate $\mathbf{B}^\theta$.

of the theorem of extremum solutions of the Laplace equation [35,36], we can say that the minimum and maximum values of the real and imaginary parts of the Fourier transform (in time) of $\mathbf{B}^\theta$ are necessarily on the surface of the continuous cylinder compartment (or its extension), for a transform along the z axis. Similarly, for a transform along the r axis, they are necessarily on that surface or at infinite. It follows that if $\mathbf{B}^\theta = f + ig$ on the surface of the cylinder (or its extension) or at the L-P and P-R interfaces, then we have $|f_1| \geqslant |f_2|$ and $|g_1| \geqslant |g_2|$ at every point in space when these inequalities are satisfied over the boundary conditions. Therefore, the absolute value of real and imaginary parts of the solution, as well as its modulus, of the first-order solution $\mathbf{B}_1^\theta = f_1 + ig_1$ are larger or equal to that of the solution $\mathbf{B}_2^\theta = f_2 + ig_2$. If this was not the case in a given point p, it would be in contradiction with the extremum value theorem, because Laplace equation is linear. Indeed, the difference between the solutions $\mathbf{B}_2^\theta - \mathbf{B}_1^\theta$ is also solution of Laplace equation for the boundary conditions $(f_1 - f_2) + i(g_1 - g_2)$. Consequently, the real and imaginary parts of the solution cannot become negative if the boundary conditions are positive.

To demonstrate that the absolute real and imaginary values are growing at each iteration (Figs. 13 and 16), we first calculate the solution using the Fourier transform along z, but assuming that, on the surface of the extended compartment, $\mathbf{B}^\theta$ is zero. In a second step, we calculate the solution using the Hankel transform along r and the continuity principle at the borders L-P and P-R. This second calculation gives new boundary conditions on the extended cylindric compartment. These boundary conditions have real and imaginary values which are necessary larger or equal (in absolute value) than the ones given for zero boundary conditions, because the finite length of Region P is now taken into account on the surface

of the extended compartment. Thus, according to above, the modulus of the second-order solution (calculated using the Fourier transform along z) is necessarily larger than that of the first-order solution, at every point in space. This reasoning will also apply to the second-order solution because the extremum value theorem implies that the modulus of the second-order approximation is larger than the modulus of the first-order approximation at every point of the interfaces L-P and P-R (Fig. 13). It follows that applying the Hankel transform with respect to r gives larger values of the boundary conditions for every point compared to the preceding order, and so on. Consequently, these successive approximations produce a series of monotonically increasing values of the modulus of $\mathbf{B}^\theta$ at every point of space. This remarkable property is a consequences of the theorem of extremum solutions of Laplace equation.

Finally, we show that this series is bounded. Indeed, the first-order solution has real and imaginary values smaller than the solution with a finite compartment, because $\mathbf{B}^\theta = 0$ on the extended compartment. Thus, according to the extremum value theorem of Laplace equation, we can write that for every point in space, the modulus of the first-order solution is smaller or equal to the exact solution of a single compartment with no extension. It follows that, for every point in space, the modulus of the first-order solution of $\mathbf{B}^\theta$ is bounded by the modulus of the exact solution of the compartment with no extension. This is also valid for the second-order solution, and so on. Consequently, the method converges to a unique solution in every point in space because we have a series which is growing and which is bounded. The unicity of the Laplace equation solution ensures that the series converges towards the exact solution of the compartment without extension.

[1] H. Weinstock, *SQUID Sensors: Fundamentals, Fabrication and Applications* (Kluwer Academic, Dordrecht, 1996).

[2] M. Hamailainen, R. Hari, J. R. Ilmoniemi, J. Knuutila, and O. V. Lousnasmaa, Rev. Mod. Phys. **65**, 413 (1993).

[3] P. P. Freitas, F. A. Cardoso, V. C. Martins, S. A. M. Martins, J. Loureiro, J. Amaral, R. C. Chaves, S. Cardoso, L. P. Fonseca, A. M. Sebastião, M. Pannetier-Lecoeur, and C. Fermon, Lab Chip **12**, 546 (2012).

[4] M. Pannetier-Lecoeur, L. Parkkonen, N. Sergeeva-Chollet, H. Polovy, C. Fermon, and C. Fowley, Appl. Phys. Lett. **98**, 153705 (2011).

[5] S. Murakami and Y. Okada, J. Physiol. **575**, 925 (2006).

[6] G. Buzsàki, C. A. Anastassiou, and C. Koch, Nat. Rev. **13**, 407 (2012).

[7] A. Destexhe and C. Bedard, Scholarpedia **8**, 10713 (2013).

[8] N. K. Logothetis, C. Kayser, and A. Oeltermann, Neuron **55**, 809 (2007).

[9] S. Gabriel, R. W. Lau, and C. Gabriel, Phys. Med. Biol.. **41**, 2231 (1996).

[10] S. Gabriel, R. W. Lau, and C. Gabriel, Phys. Med. Biol. **41**, 2251 (1996).

[11] C. Bédard, H. Kröger, and A. Destexhe, Phys. Rev. Lett. **97**, 118102 (2006).

[12] M. Bazhenov, P. Lonjers, P. Skorheim, C. Bedard, and A. Destexhe, Phil. Trans. R. Soc. A **369**, 3802 (2011).

[13] C. Bédard, S. Rodrigues,, N. Roy, D. Contreras, and A. Destexhe, J. Comput. Neurosci. **29**, 389 (2010).

[14] N. Dehghani, C. Bédard, S. S. Cash, E. Halgren, and A. Destexhe, J. Comput. Neurosci. **29**, 405 (2010).

[15] C. Bédard and A. Destexhe, Phys. Rev. E **84**, 041909 (2011).

[16] J. J. Riera, T. Ogawa, T. Goto, A. Sumiyoshi, H. Nonaka, A. Evans, H. Miyakawa, and R. Kawashima, J. Neurophysiol. **108**, 956 (2012).

[17] W. Rall, Biophys. J. **2**, 145 (1962).

[18] W. Rall, *The Theoretical Foundations of Dendritic Function* (MIT Press, Cambridge, MA, 1995).

[19] U. Mitzdorf, Physiol. Rev. **65**(1), 37 (1985).

[20] C. Bédard and A. Dextexhe, Phys. Rev. E **88**, 022709 (2013).

[21] H. C. Tuckwell, *Introduction to Theoretical Neurobiology: Linear Cable Theory and Dendritic Structure* (Cambridge University Press, Cambridge, 1988).

[22] D. Johnston and S. M. Wu, *Foundations of Cellular Neurophysiology* (MIT Press, Cambridge, 1995).

[23] C. Koch, *Biophysics of Computation* (Oxford University Press, Oxford, 1999).

[24] K. S. Cole and R. H. Cole, J. Chem. Phys. **9**, 341 (1941).

[25] L. D. Landau and E. M. Lifshitz, *Electrodynamics of Continuous Media* (Pergamon Press, Moscow, 1984).

[26] C. Bédard, H. Kröger, and A. Destexhe, Phys. Rev. E **73**, 051911 (2006).

[27] C. Bédard and A. Destexhe, Biophys. J. **96**, 2589 (2009).

[28] M. George, S. Lisanby, and H. Sackeim, Arch. Gen. Psychiatry **56**, 300 (1999).

[29] S. J. Salon and M. V. K. Chari, *Numerical Methods in Electromagnetism* (Academic Press, New York, 1999).

[30] J. DeFelipe, P. Marco, I. Busturia, and A. Merchàn-Pérez, Cereb. Cortex **9**, 722 (1999).

[31] A. M. Cassarà, G. E. Hagberg, M. Bianciardi, M. Migliore, and B. Maraviglia, NeuroImage **39**, 87 (2008).

[32] S. S. Nagarajan and D. M. Durand, IEEE Trans. Biomed. Eng. **43**, 304 (1996).

[33] H. Bateman, *Higher Transcendental Functions* (California Institute of Technology, Pasadena, 1981), Vol. 1.

[34] H. Bateman, *Higher Transcendental Functions* (California Institute of Technology, Pasadena, 1981), Vol. 2.

[35] V. I. Smirnov, *A Course of Higher Mathematics* (Pergamon Press, Moscow, 1964), Vol. 2.

[36] V. I. Smirnov, *A Course of higher Mathematics* (Pergamon Press, Moscow, 1964), Vol. 5.